

Design and control of a low profile electromagnetic actuator for foldable pop-up mechanisms

M. Salerno¹, F. Zuliani¹, A. Firouzeh and J. Paik

Abstract—Thin foldable origami mechanisms bring miniaturization and reconfiguration of complex structures allowing large volumetric change, low cost and versatility. Many applications require small robots with multiple capabilities including movement, sensing and communication. One of the major design constraints in these systems is miniaturization, in particular actuator down-scaling. To meet the challenges, researchers have focused both on investigating designs that use high power to size ratio actuators as well as defining novel fabrication methods that aid reduced size component integration.

This paper presents a novel approach for designing and controlling a low profile electromagnetic (EM) actuation system that can provide high speeds and easy control. Additionally, the system can be embedded in miniaturized foldable mechanisms. We report here the modelling of the low-profile EM actuator and the design methodology; further, the fabrication of a 3-cm wide, 1.4 mm thick prototype and real case scenario testing were executed. Our extensive test results verify the position control performance and validate the thermo-mechanical model in terms of expected steady state temperature and dependency by actuation frequency.

Keywords:

Foldable system, electromagnetic actuator, planar coils, origami platform, low profile power transmission

1. INTRODUCTION

Robots are now used in everyday life, not only for repetitive and tiring tasks, but for diverse human interaction applications. One of the major design constraints of robotics systems is miniaturization. Many applications require small robots with multiple capabilities such as moving, sensing and communicating. In other cases, switching from a compact, folded configuration to a 3D one is desired. Moreover, a variety of goals can be reached through space reduction design; an example is efficient robot locomotion and cooperation in complex environments [1, 2, 3]. To face the miniaturization challenge, researchers focus on investigating designs that use high power to size ratio actuators as well as defining novel fabrication methods that aid reduced size component integration. In some studies, compact robots were obtained by closely integrating sensors and actuators within robot body [4, 5]. Others focused on fabrication; using novel manufacturing methods, such as layer-by-layer technique [6], allows embedding thin actuators and sensors into flat systems [6, 7]. The use of shape memory materials eases system miniaturization [8, 9] but they have the drawback of low actuation speed and control complexity.

While simple folding geometries are easy to miniaturize using Smart Composite Microstructure (SCM), shrinking complex 3D mechanisms remains challenging. A successful approach to face this challenge is to employ origami-inspired folding design for assembling and reconfiguration. The folded state can be used to either ease manufacturing [10] or to reduce

mechanism size to lower cost of transportation [11]. The challenge we face in this system is designing an actuation scheme that can be embedded in the miniaturized foldable mechanisms while providing high speeds and easy control. The actuator is one of the most difficult components to scale down while maintaining its functionality.

In this work, we present a low profile electromagnetic (EM) actuator designed for embedding in a foldable structure for high performing self-contained shape-shifting devices. The miniaturization (under cm scale) of EM systems is broadly investigated and interesting from an energetic point of view [12-14]. The main advantages of the system we propose are its wide range of motion and the simple manufacturing method which is not usual for EM systems [15]. The main challenge we face is the overall design limitation to keep the system as thin as possible while guaranteeing desired actuation performance. Examples of similar system designs are found in literature for voice coil systems [16]. Most of the miniature EM systems investigated though use only the vertical component in coaxial magnet-coil interaction giving very small strokes [17-18]. Other systems however, use more efficient methods to move magnets on a surface achieving wider strokes. Nevertheless, the assembly results in quite complex and bulky (over 10 cm) structures [19-21].

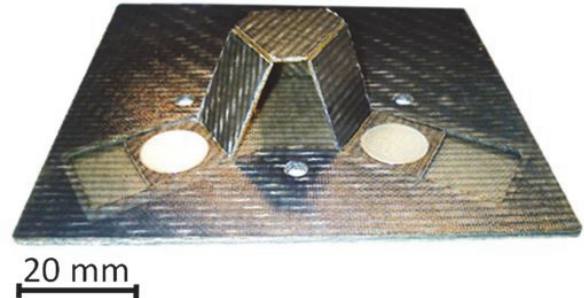


Figure 1: Pop-up, origami inspired, low profile mechanism presented by the authors in [22]

Previous work from Salerno et al. [22] introduced a foldable system where the EM actuation is integrated using layered low-profile manufacturing technique. The system was composed of a permanent magnet constrained in a rail and moved by interaction with a coil pair. The copper multilayer coils are etched onto a flexible Pyralux substrate and embedded in a carbon fiber structure. The investigated design is challenging due to the multidisciplinary approach required for reducing the size and improving the thermal behavior of the system while keeping the desired actuation characteristics.

In this paper, we present a design framework to define the actuator parameter values to reach a desired performance. This framework specifically delineates the coils features to achieve set forces while keeping the systems temperature under a specific limit so allowing continuous actuation. Furthermore, we integrate sensors on top of the structure but maintain a

¹ These authors contributed equally to this work.

thickness of less than 1.7 mm. We use sensory feedback as control methodology for the proposed actuator.

The major contributions of the presented work are:

- The mm-scale novel planar EM actuator design.
- The thermo-mechanical model of the actuator.
- The design framework of the EM actuator with respect to the required thermomechanical performance.
- The actuator position control based on sensory feedback.

2. ANALYTICAL METHODS FOR THE PLANAR EM ACTUATOR

The linear EM actuator considered in this work is made from multiple functional layers: the coil layer is used to generate the magnetic field needed for actuation; the permanent magnet is assembled on the moving part of the actuator; the rail layers constrain the motion of the moving part and the structural layer provides the mechanical stability. Figure 2 shows the stacked system in (a) and the different layers composing the system in (b). The actuator was fabricated using traditional PCB process to obtain the planar coils, using Smart Composite Microstructure manufacturing technique for the actuator body. The process is described in detail in the authors' previous works [22].

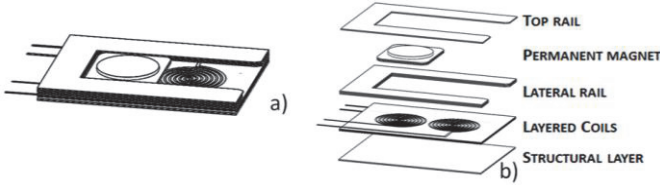


Figure 2: Construction of the actuator. The stacked layers give an overall thickness of less than 3 mm (a). The exploded view of the actuator shows the carbon fiber structure with the rail, the coils and the slider with an embedded permanent magnet (b).

At the base of the design methodology for the proposed low profile EM actuator are the mathematical models that describe electromagnetic interactions and temperature variations of the system. First, we present a model to calculate the magnetic force between the coil system and the permanent magnet (Eq. 3) and then a model for the transient and steady-state temperature of the system at different input powers (Eq. 8). These models are used to design the coils. In the following Sections, we describe the physical assumptions we make and the analytical definitions used.

2.1 Magnetic Force Model

The magnetic force model is derived from the interaction between the magnetic field produced by the thin coils and the permanent magnet. The permanent magnet, with specific magnetization, is modeled as a coil driven by an equivalent current. The magnetic field is derived from the Biot-Savard law [23] which gives the magnetic field produced by a wire driven by a current I at position \vec{r} :

$$\vec{B}(\vec{r}) = \frac{\mu_0}{4\pi} \int \left(\frac{I d\vec{l} \times \vec{r}}{r^3} \right) \quad (1)$$

Where μ_0 is the magnetic permeability in vacuum and $d\vec{l}$ is the wire element. We use (1) with the Archimedean spiral

parametrization of the coils and we obtain the magnetic field. The final equation to compute the magnetic field of the thin coil is reported in (2).

$$\begin{aligned} B_x(\vec{r}) &= \frac{\mu_0 I}{4\pi} \int \frac{z \left(i_r + \frac{\omega\theta}{2\pi} \right) \cos(\theta)}{\left(x - \left(i_r + \frac{\omega\theta}{2\pi} \right) \cos(\theta) \right)^2 + \left(y - \left(i_r + \frac{\omega\theta}{2\pi} \right) \sin(\theta) \right)^2 + z^2} \\ B_y(\vec{r}) &= \frac{\mu_0 I}{4\pi} \int \frac{z \left(i_r + \frac{\omega\theta}{2\pi} \right) \sin(\theta)}{\left(x - \left(i_r + \frac{\omega\theta}{2\pi} \right) \cos(\theta) \right)^2 + \left(y - \left(i_r + \frac{\omega\theta}{2\pi} \right) \sin(\theta) \right)^2 + z^2} \\ B_z(\vec{r}) &= \frac{\mu_0 I}{4\pi} \int \frac{z \left(i_r + \frac{\omega\theta}{2\pi} \right) (x \cos(\theta) - y \sin(\theta)) + \left(i_r + \frac{\omega\theta}{2\pi} \right)^2}{\left(x - \left(i_r + \frac{\omega\theta}{2\pi} \right) \cos(\theta) \right)^2 + \left(y - \left(i_r + \frac{\omega\theta}{2\pi} \right) \sin(\theta) \right)^2 + z^2} \quad (2) \end{aligned}$$

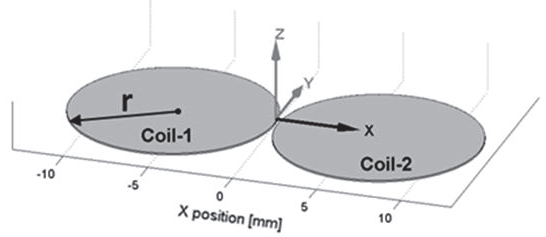


Figure 3: Schematic of the coil positions and the reference axis used in the calculation of magnetic forces.

In this study we are concerned with the force along the x axis that drives the slider inside the rail (Figure 3). The component on the Z axis could be used in a further study to take into consideration the friction between the rail and the magnet (Figure 3). To calculate the magnetic forces we model the permanent magnet as a coil of the same shape with equivalent surface current density [23, 25]. We discretize the magnet surface into surface elements (a_n) and define the surface current density as a cross product between the magnetization \vec{M} and the vector normal to each surface element \vec{a}_n . Only the radial surface S of the cylinder is taken into consideration, as the top and bottom sides have their normal vector parallel to the magnetization, which gives zero contribution. The interaction force between the magnetic field produced by the coil and the so modelled magnet is, therefore, described in Equation (3).

$$\vec{F} = \int_S \vec{M} \times \vec{a}_n \times \vec{B}_{coil} \quad (3)$$

We then compute the magnetic force applied to the magnet using numerical methods to obtain the magnetic force in the whole range of motion. Here we discretized the surface of the magnet into 64 elements and the height of the magnet in 3 layers to have more accurate results. Further discretization did not bring appreciable changes to the computed values. Since the component of the magnetic force along the x direction at a specific powering current depends on the position of the magnet on the rail, we calculated a function defining the current required (I_r) at each magnet position, to have a constant force along the x direction. To continue, we defined a function that relates coil current and magnet position to produce a constant horizontal force. The function was obtained by calculating, with the analytical force model, the current applied to the coil when the force applied to the

magnet is constant. The function obtained is reported in Figure 4.

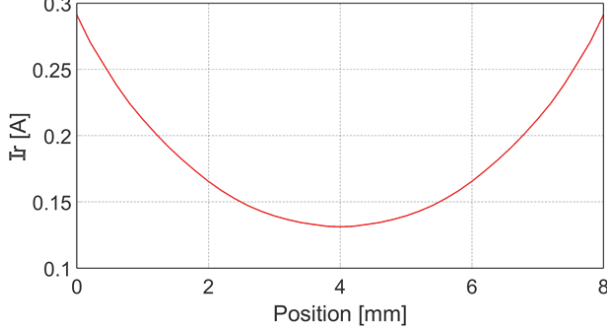


Figure 4: Function compensating the magnetic force vs position non-linearity. The most efficient point is in between the two coils as the force is fully horizontal and therefore less current is needed to achieve a defined force. The highest current applicable to the coils (0.3 A) refers to the border of the workspace.

2.2. Thermal Dissipation Model

To estimate the temperature of the system during operation, we set a thermal dissipation model of the actuator to face the challenge of identifying the main parameters influencing actuator steady state temperature. In the thermal model, we approximated the coil as a copper cylinder, laminated on kapton. The heat generated by the coil is transferred radially in the structure and is dissipated to the environment. Based on the higher thermal conductivity of the copper (385 W/mK) compared to the thermal conductivity of the Kapton (0.12 W/mK) and glass fiber layer (1.3 W/mK), conduction through the copper sink attached to the structure is dominant. We approximated the problem as a thermal problem with axial symmetry presented in Figure 5.

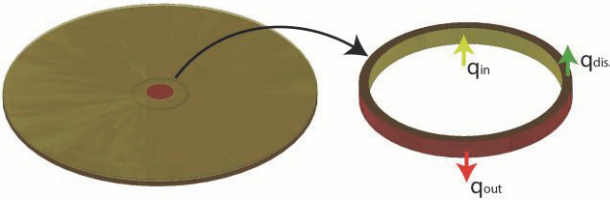


Figure 5: Equivalent thermal models. The conduction through the copper sink is dominant and is the only mode of radial heat transfer considered in this study. We study an equivalent axial symmetric heat transfer problem here.

The main motivation for simplifying the thermal problem was to achieve a problem with a simple solution, possibly closed form that can be used in the design process. We considered the following approximations for studying the thermal behavior:

- 1- Axial symmetry.
- 2- The heat transfer in the radial direction is dominated by the conduction in the copper layer.
- 3- The temperature gradient in the direction of the thickness is neglected and only dissipation from the bottom surface or the sink is considered.

- 4- The heat dissipation to the environment is modeled by a linear function with coefficient h , which is determined using experimental results.

Based on these assumptions, the energy equation for the radial element of Fig 5 is written as:

$$q_{in} - q_{out} = q_{dis} + \frac{\partial T}{\partial t} d(mc) + \frac{q_{gen}}{\pi r_{coil}^2 b} b(2\pi r dr) \quad (4)$$

where $q_{in} - q_{out}$ is the heat transfer to the element through conduction and is calculated as:

$$q_{in} - q_{out} = kb(2\pi r dr) \left(\frac{\partial^2 T}{\partial r^2} + \frac{1}{r} \frac{\partial T}{\partial r} \right) \quad (5)$$

k is the thermal conductivity, b is the thickness of the conductive layer (here we considered heat transfer through the copper sink), and r is the distance of the element from the center of the coil. q_{dis} in equation (4) is the heat dissipation to the environment which is modeled as:

$$q_{dis} = h(2\pi r dr)(T - T_{\infty}) \quad (6)$$

in which h is the coefficient of heat dissipation to the environment determined using characterization test. The second term on the right side of equation (4) represents the energy required to increase the temperature in the element which can be written as:

$$\frac{\partial T}{\partial t} d(mc) = \frac{\partial T}{\partial t} b(2\pi r dr)(\rho c)_{equ.} \quad (7)$$

$(\rho c)_{equ.}$ represents the equivalent thermal capacity of the layers. We considered only the mass of copper as the heat capacitance based on the rather insulating properties of polyimide and glass fiber. Finally, the last term on the right side of equation (4) represents the joule heating in the coil. The heat generation has the following form:

$$q_{gen} = \begin{cases} \frac{v^2}{R(1+\alpha(T-T_0))} \text{ or } I^2 R(1+\alpha(T-T_0)), & r < r_{coil} \\ 0, & r > r_{coil} \end{cases} \quad (8)$$

α in this equation represents the electrical resistance's thermal coefficient. The two representations correspond to the heat generation in a coil with constant voltage and with constant current (magnetic field).

Using (4)-(8), we can analyse the transient and the steady-state behaviour. To obtain a closed form for the steady state solution, the problem is further simplified by considering heat generation in a circular section with a diameter half of the coil diameter. Considering this the problem can be further simplified into the following ODE:

$$\frac{\partial^2 \theta}{\partial r^2} + \frac{1}{r} \frac{\partial \theta}{\partial r} - m^2 \theta = 0, \quad m^2 = \frac{h}{kb}, \quad \theta = T - T_0 \quad (9)$$

This is Bessel equation of order zero. In this equation θ represents the temperature difference between the sink and the environment. As for the boundary condition, we considered the following:

$$\begin{cases} q|_{r=\frac{r_{coil}}{2}} = \frac{V^2}{R(1+\alpha(T-T_0))} \text{ or } I^2 R(1+\alpha(T-T_0)) \\ q|_{r=r_{out}} = 0 \end{cases} \quad (10)$$

The corresponding solution of the above problem has the following form [24]:

$$\frac{\theta}{\theta_b} = \frac{I_0(mr)K_1(mr_2)+K_0(mr)I_1(mr_2)}{I_0(mr_1)K_1(mr_2)+K_0(mr_1)I_1(mr_2)} \quad (11)$$

In (11), I_i and K_i are Bessel function of the first and second kind, respectively, and i represents the order of the function. The temperature of the inner boundary is calculated according to:

$$\theta_b = \frac{q_f}{2\pi k r_1 t m} \frac{K_0(mr_1)I_1(mr_2)+I_0(mr_1)K_1(mr_2)}{K_1(mr_1)I_1(mr_2)-I_1(mr_1)K_1(mr_2)} \quad (12)$$

The closed form solution of equation (11) is used in the design process while the numerical solution of the PDE presented in equations (4)-(8) is used to study the thermal transient response.

2.3. Coil design

In this work we define a design methodology to target desired characteristics of the actuator. Some of the design criteria are to avoid overheating for specific working conditions, actuator output force and confining power needs.

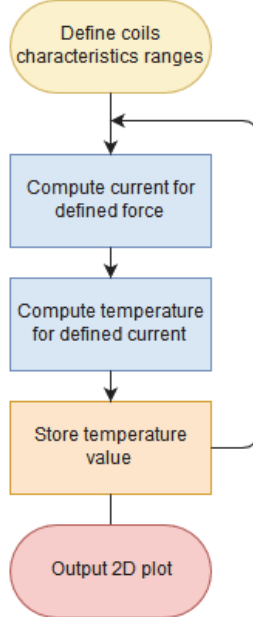


Figure 6: Flowchart for defining the actuator coil geometry. The first step is the definition of the investigated range for the various characteristics of the coil. The processing part is a loop which computes the steady temperature of the system under action with the analytical model for the whole range of different characteristics. This gives a complete mapping of the temperature as a function of the size of the coils and the wires.

The coil design parameters include the number of single coils that are stacked to obtain a multi-layer coil, the thickness of the copper in the laminates used and the number of turns of each coil. The number of turns is inversely proportional to the width of the winding; together these parameters define the electrical resistance of the coil. Further, to keep a constant force applied to the magnet, the current has to be modified in agreement with the number of layers stacked and the number of turns of each coil.

To define a design framework, the magnetic force and thermal dissipation analytical models presented in Section 2 are used to simulate the steady temperature reached while the coil is actuated for each set of characteristics described above. The obtained values are then plotted to better understand the relation between steady-state temperature and parameter variation.

3. EM ACTUATOR PROTOTYPE CONTROL METHODS

Once we manufactured the EM actuator prototype, we defined a control strategy for moving it within its workspace using a specific frequency or into specific locations.

3.1 Position feedback

The control of EM actuators requires proper sensory feedback. In this Section we describe the approach we followed to obtain the position information. One of the priorities in the proposed actuator design is to achieve a low profile structure; for this reason, we embedded the sensors in the layers that compose the rail. The magnet position is sensed using two Hall-effect sensors (SS495A, Honeywell), placed on the side of the rail (as Figure 9 reports), measuring the magnetic field produced by the permanent magnet. By using two sensors, it is possible to define the relation between magnet position and readings. The specific arrangement of the sensors allowed us to have a linear relation.

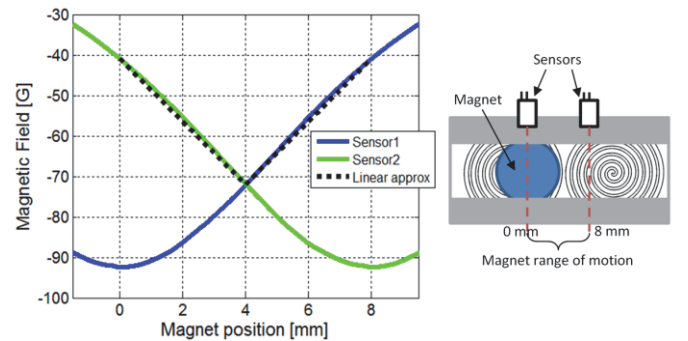


Figure 7: Output of the two Hall effect sensors placed on top of the actuator. The magnetic field changes depending on the position of the magnet along the moving range. The dotted lines are the two approximation functions used for position computation (coordinates illustrated in Fig. 3).

The output of the sensors depends on the position of the magnet as shown on Figure 7. A linear approximation (dotted lines) was used, thus simplifying the position calculation. The sensing methodology was defined using Comsol Multiphysics simulation results. Once we built the prototype and executed the sensing, we calibrated the sensor readings by retrieving the magnetic fields read by the sensors for specific positions of the actuator (0, 4 and 8 respectively). We use these values in

the linear transfer function; the calibration procedure took place using three specific positions set manually with a mechanical spacer of respectively 0, 4 and 8 mm.

3.2. Control of EM actuator

To control the actuator, we have to track its position and compensate for its non-linearity. Further, the control law we implement should require low computational time to preserve actuator bandwidth. The actuator's non-linearity is described in Fig. 4. The position along the x axis where the horizontal force is maximum, is the midpoint of the range of motion, in-between the two coils, as the force has only horizontal component. The positions where the horizontal force is minimum correspond to the coils' centers where the force has the sole vertical component. The control method we implemented is a simple PID controller with a numerical low-pass filter to reduce the noise on the sensors and a current compensation function of position, to have constant control conditions over the whole actuation range.

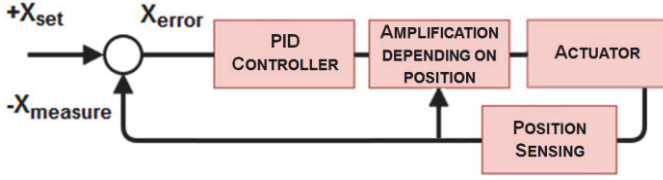


Figure 8: The EM actuator controller. The position sensing is performed with Hall-effect sensors, whose output is low-pass filtered. The position is interpolated with the approximation function shown in Figure 6. The PID was tuned to move the magnet towards the goal position. This output value is then multiplied by the compensation factor to apply a constant force to the magnet at any point of the motion range.

4. BENCHMARKING AND TEST DESCRIPTION

In this Section, we report the description of the test executions. The tests were designed to highlight and verify analytical methods and the design pipeline.

4.1 Hardware description

The actuator is composed of two 10-layer coils, a carbon fiber rail placed on top of them and a magnet constrained in a Pyralux structure that is coupled to the rail in a prismatic joint, as reported in Figure 9. The electronics we used to drive the coils are composed of an Arduino Mega (PWM frequency 32kHz) connected to a dual full-bridge driver L298, (STMicroelectronics, IT). The sensory feedback is composed of the two hall-effect sensors already mentioned.

4.2. Test descriptions

The tests were performed by recording the system's changes in temperature using a thermal camera (FLIR A5). The motions of the magnet in time were recorded using a high speed camera and processed with the software Kinovea. In the experiments analyzing system power consumption and heat power generated, we used an oscilloscope (Tektronix DPO 3014, USA) to record the current flowing in the coils.

5. RESULTS

In this Section, we report the results of the tests that were conducted to validate the proposed design methodology and evaluate the performance of the actuator.

5.1 Analytical model validation

To validate the force analytical model, we compared analytical results with FEM simulations performed using Comsol Multiphysics. To verify the magnetic force model, we set a simple one-dimensional problem with a magnet on top of a coil and computed the interaction force, depending on the distance between the two. Figure 10 shows the FEM and analytical result comparisons.

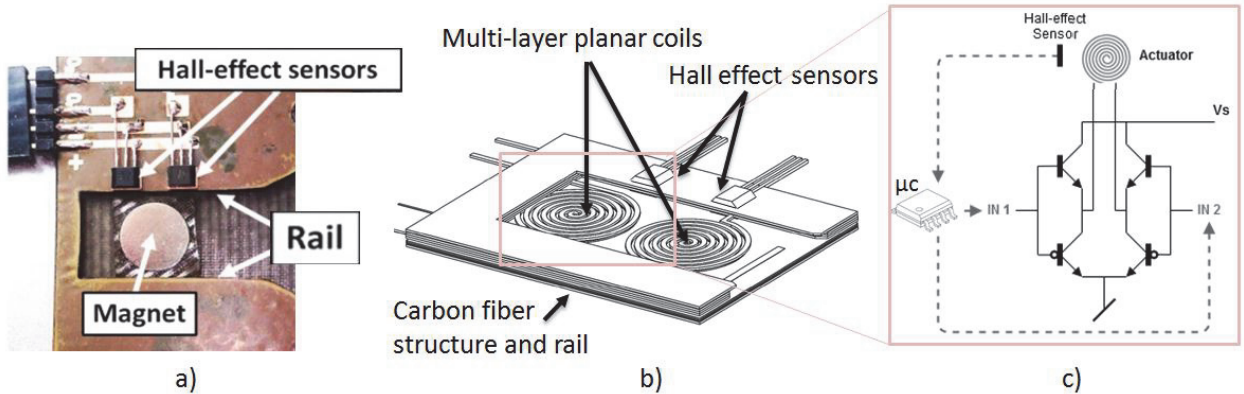


Figure 9: The EM actuator prototype. Mainly built from carbon fiber, the structure includes three rails for actuating a foldable mechanism (a). The left rail has a magnet in a Pyralux structure placed in the middle of the actuation range. Two Hall-effect sensors placed over the structure give the magnet position feedback for the actuation of the mechanism. Schematic detail of the prototype's left rail (b). The figure shows the carbon fiber structure, the planar coils and the sensors. Electronic schematic of the circuit used for actuator control (c). The microcontroller reads the Hall effect sensor outputs and calculates magnet position; it sets the PWM signals which control the dual full-bridge driver L298 (STMicroelectronics, IT), driving the coils' current.

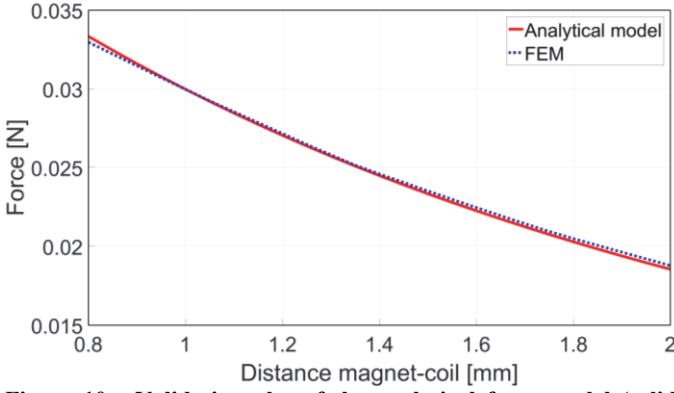


Figure 10: Validation plot of the analytical force model (solid line) applied by the current driven coils to the magnet, with a Finite Element Model (dotted line). The models consider the simple case of a cylindrical magnet placed on top of the cylindrical coil with concordant magnetization axis; errors were lower than 3%.

The thermal dissipation model was validated experimentally by recording the temperature of a coil with a thermal camera. The convection factor of the analytical model was obtained by fitting the analytical model to the experimental results, in particular to give a good approximation of the temperature after a long period of actuation (i.e. > 30 s). Figure 11 shows the experiment results compared to the analytical model.

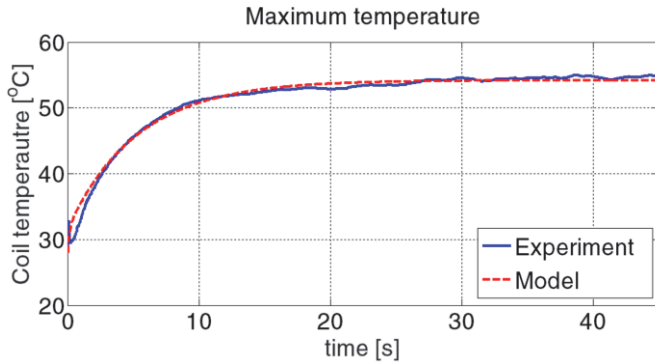


Figure 11: Coil temperature from the Model (dotted line) and the experiment (solid line). Conditions: ($R = 126.9 \Omega$, $I = 0.06$ A); errors were lower than 5%.

5.2. Coil design process

Thermal effects are not negligible in most actuators. One of the goals of this work is to predict the working temperature of the novel low profile EM actuator. To verify the proposed actuator design method, we followed the methodology proposed in the Section 2.3, designing a coil system as trade-off for fabrication ease (number of layers < 10) and steady state temperature (maximum temperature in working conditions $< 150^\circ\text{C}$).

As input for the design problem, we considered the width of the copper wire and the number of layers used in the coil stack. The ranges of the input parameters were chosen as follows: number of layers between 1 and 15 (where 15 was the upper limit to contain the thickness of the actuator); width of the copper wires between $50 \mu\text{m}$ (smallest path achievable with the resolution of the photoresist used) and $120 \mu\text{m}$ (which is a value commonly used in standard electronic components).

Figure 12 reports the maximum temperature of the system in steady-state when a constant force is applied to the magnet. The maximum temperature of the system is the temperature at the center of the coil.

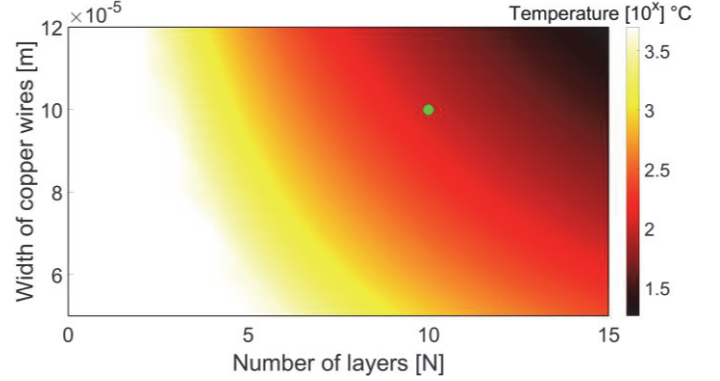


Figure 12: Mapping of the system's temperature according to the analytical thermal dissipation model. The output model values are defined for a steady-state under continuous actuation depending on the width of the copper wires and the number of coil layers stacked. The selected working point (circle) chosen has wire widths of $100 \mu\text{m}$ and a 10-layer stack. It gives a theoretical steady temperature of 150°C .

The coil parameters selected represent a good compromise in terms of the temperature of the system and ease of manufacturing. The manufactured coil has $100 \mu\text{m}$ -wide wires and 10 layers. This configuration gives a steady-temperature of around 150°C , using an average current of 0.3 A that would generate a constant magnetic force of 17 mN.

Number of layers	Copper path width [μm]	Average input current per coil [mA]	Force [mN]	Steady T [$^\circ\text{C}$]
10	100	300	17	150

Table1: Coil design parameters and actuator model performance

5.3. Position control

We tested the capabilities of the actuator in several experiments to characterize their performance. The first test performed was a sequence of steps with amplitude of 1 mm for each step. Figure 13 shows the command and actuator response comparison. Actuator response was detected using a high speed camera (Sony RX100 IV) and post processing was executed using the software Kinovea. A numeric low-pass filter was implemented to reduce the noise on the sensors.

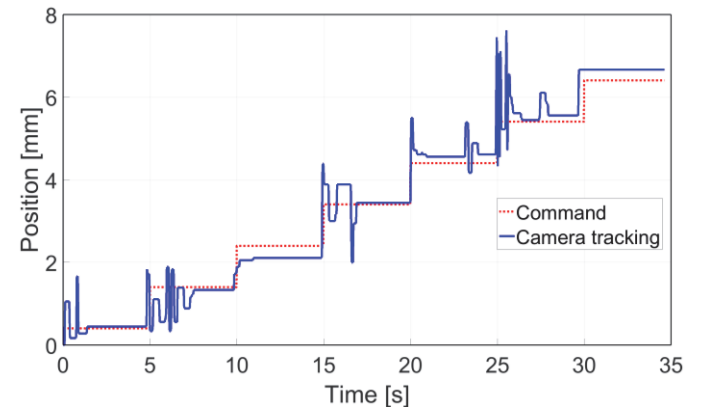


Figure 13: Controller validation with a stair input (dotted line) with an amplitude of 1 mm and a frequency of 0.2 Hz. The output response (solid line) shows the actual position of the magnet with time. Apart from the overshoots during the position transitions, the magnet reaches well the goal position at each step.

The second test performed is the same as the first but with a 4.75 Hz sine command to focus on the dynamical response and avoiding the Coulomb friction effects.

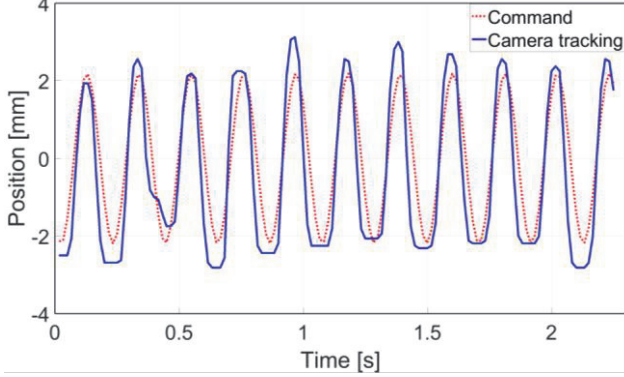


Figure 14: Controller validation with a sine input (dotted line) with amplitude of 4 mm and a frequency of 4.75 Hz. The output response (solid line) shows the actual position of the magnet in time. The controller behaves better than with the stair input as the motion is seen only as dynamic, which reduces the friction between the moving magnet and the rail. The few overshoots can be considered due to friction inhomogeneity along the range of motion of the rail.

5.4. Actuation Frequency vs Power Consumption

EM actuators are often preferred for their high speed, simple control and compact design. To characterize the designed prototype, we tested the actuation frequency achievable and the powering required for specific frequencies. These values can be used as a reference whenever the actuator is coupled to a mechanism. Figure 15 shows the tested frequencies (round points) at which the actuator's electrical power consumption was measured.

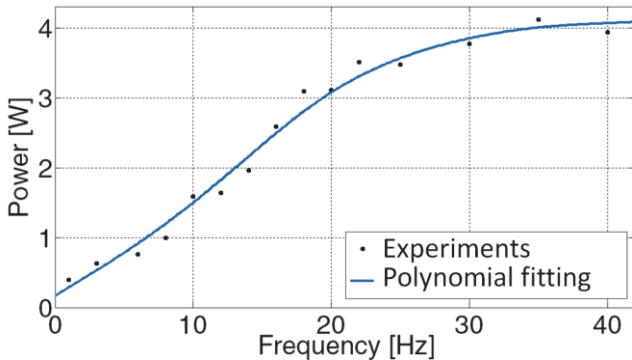


Figure 15: Power consumption depending on the frequency of a sine motion along the full range of the rail. The circles show each measure and the full line is an interpolation of the tested points along the full range of frequencies. The dependency between the frequency and the power consumption is considered as linear between 1 and 20 Hz. Frequencies higher than 20 Hz give constant power, showing the working limit of the actuator, which cannot handle higher frequencies.

5.5. Temperature changes in working conditions

To verify experimentally the thermal model and the design methodology, we measured actuator temperature increase at different working frequencies.

The last test executed evaluates temperature rise during sinusoidal actuation at 1 Hz, 3 Hz and 10 Hz. The temperature changes were measured with a thermal camera. The output power of the actuator was recorded with an oscilloscope; its average value with time was used as equivalent power for the analytical model. Figure 16 shows an increase of the steady-state temperature with increases in actuation frequency.

Compared to Figure 11, where constant current was applied to the coil, in the experiments presented in Figure 16 the controller applies PWM with varying duty cycle to control the position of the magnet in its cyclic motion. In this case, we used the average power consumption as the input for the model. With this input, we can predict the steady state response rather closely. The transient response however is less accurate, resulting from the varying input energy to the coils.

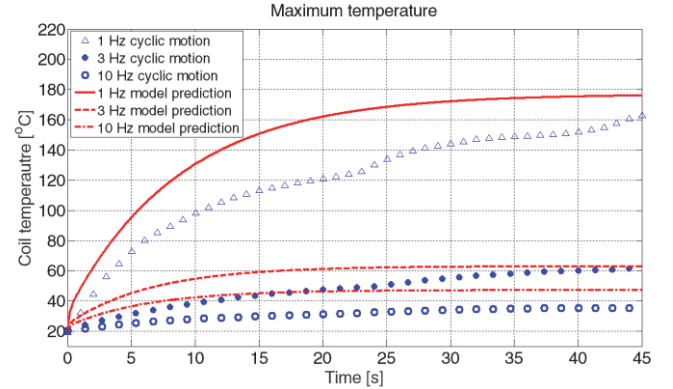


Figure 16: Validation of the analytical model (solid lines) for the thermal dissipation under sine actuation of the magnet with experimental results (rounds and triangles). Due to the unsteady friction between the magnet and rail, the experiments report higher temperatures than the model. However, the trend is well described by the analytical model and can be used to predict the system's temperature.

Figure 17 shows the thermal images of the system, giving an overview of the heat distribution when a 10 Hz motion is executed. As expected, the temperature is higher in the center of the coil and becomes lower as we radially move away. The heat remains located mainly on the coils themselves. The presented experimental results match well the theoretical values, thus verifying the validity of the followed approach and the performance of the temperature prediction.

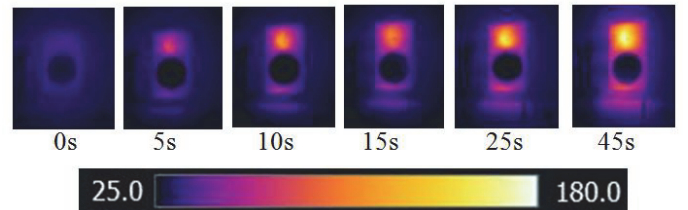


Figure 17 : Visualization of the coils' temperature distribution during actuation using a thermal camera. As expected, the center of the coil is the hottest part during actuation and the heat stays focused on the copper pattern as it is a good temperature conductive material. The temperature of the surroundings of the coil increase slowly but the top of the coil would be the most

interesting for heat sink investigations. The temperature is measured in °C.

6. DISCUSSION AND CONCLUSION

The motivation of this work is the design of an EM actuation system that can be embedded in miniaturized foldable mechanisms, such as pop-up mechanisms, that at the same time can provide high speeds and easy control. To achieve this goal we proposed a methodology to design the coils of a low-profile EM actuator, estimating the working temperature during actuation. We developed the analytical models that provide an accurate estimation of magnetic forces and temperature (less than 10 % error) and we used the models to design a coil system performing 1-10 Hz motions within the expected temperature limits, defined as lower than 150°C. The thermal dissipation model in particular required tuning of the convection factor by comparing it to the experimental temperature behavior. The validation of the two analytical models confirmed their realistic approximation of the system to be used in the coil design process. We chose an actuator design with 10 layers of coils and conductors 100 μm wide in agreement with the design method. This configuration represents a trade-off between minimizing the maximum temperature of the system at steady-state under continuative actuation, maintaining low thickness of the actuator to keep its low-profile characteristic and finally minimizing the necessary current to make it usable with widely used electronical components. We expected from this selection, a steady-temperature of around 150°C as maximum temperature to not damage the actuator. We were able to verify this value experimentally by performing continuative actuation for several minutes. We then implemented a control method that involves embedding Hall-effect sensors into the structure, keeping the thickness of the system low. The successful implementation of the controller allowed regulation of the position of the actuator and its speed, although performing slow motion was challenging due to the high Coulomb friction present in the actuator. In the future, employment of materials with lower friction coefficients should improve this aspect.

We evaluated the actuator motion over a range of frequencies (5 to 25 Hz), which shows linear dependency to the powering. The plateau after 25 Hz indicates the maximum rating of the produced prototype. Computations for continuous use give a maximum of 2 W of powering to keep the temperature under the design limit. These values are reasonable for portable devices in terms of power consumption and temperature. The maximum frequency that could be used for continuative actuation is therefore around 10 Hz. This frequency could be improved in future by lowering the friction between the rail and the magnet using other materials, or by increasing the number of coils along the rail to improve the direction of the magnetic force applied to the magnet at any position. The achieved motion frequency could allow us to use the actuator for haptic applications. The defined model approximates the coils' temperature increase during continuative sinusoidal actuation satisfactorily,

although there is a slight underestimation of the temperature (<15%). This is probably due to the powering value used for the analytical model, which is the average value of the current over time and not the exact thermal power generated; taking this into consideration would give a better temperature approximation. The methodology proposed to estimate the thermal behavior of electromechanical systems to keep continuative actuation is convincing, as our predictions were realistic and allow us to effectively design an actuator that could fulfill the initial goal of continuative actuation.

In summary, in this work we present a novel approach to design and control a low-profile EM actuator system. Our design can provide high speeds and easy control and we show it can be embedded in miniaturized foldable mechanisms. We successfully modeled the low profile EM actuator and we defined its design methodology. The fabricated prototype was tested in real case scenarios and position control performance was validated.

The proposed design process could be transferred to other systems using layered coil design, or more widely to low-profile electromechanical systems. The embedded control strategies could also be implemented for other low-profile automated systems.

ACKNOWLEDGEMENTS

This work was supported by the Swiss National Science Foundation through the National Center of Competence in Research (NCCR) Robotics and by the SNF in the framework of the project START (Surface for TAngible RealiTy).

REFERENCES

- [1] Wolfgang Fischer, Gilles Caprari, Roland Siegwart, Igor Thommen, Wolfgang Zesch, Roland Moser, (2010) "Foldable magnetic wheeled climbing robot for the inspection of gas turbines and similar environments with very narrow access holes", *Industrial Robot: An International Journal*, Vol. 37 Iss: 3, pp.244 – 249
- [2] Jeremy M. Morrey, Bram Lambrecht, Andrew D. Horschler, Roy E. Ritzmann, Roger D. Quinn "Highly mobile and robust small quadruped robots" (2003) *Intelligent Robots and Systems Proceedings. 2003 IEEE/RSJ International Conference*
- [3] Kushleyev, A., Mellinger, D., Powers, C. et al. Towards a swarm of agile micro quadrotors (2013) *Auton Robot* 35: 287. doi:10.1007/s10514-013-9349-9
- [4] C. Suh, J. Condal Margarit, Y. Seong Song, Jamie Paik Soft Pneumatic Actuator skin with embedded sensors (2014) *IEEE/RSJ International Conference on Intelligent Robots and Systems (IROS)*
- [5] Selim Ozel, Nehir A. Keskin, Darien Khea, Cagdas D. Onal A precise embedded curvature sensor module for soft-bodied robots (2015) *Sensors and Actuators A: Physical* Vol. 236
- [6] A. Firouzeh, Y. Sun, H. Lee and J. Paik; Sensor and actuator integrated low-profile robotic origami (2013) *IEEE/RSJ International Conference on Intelligent Robots and Systems (IROS)*
- [7] A. Firouzeh, J. Paik Robogami: A Fully Integrated Low-Profile Robotic Origami (2015) *J. Mechanisms Robotics* 7
- [8] E. Hawkesa, B. An, N. M. Benbernou, H. Tanaka, S. im, E. D. Demaine, D. Rus, R. J. Wood Programmable matter by folding (2010) *Proceedings of the National Academy of Sciences*
- [9] S. Felton, M. Tolley, E. Demaine, D. Rus, R. Wood A method for building self-folding machines (2014) *Science* Vol. 345
- [10] Samuel M. Felton ; Michael T. Tolley ; Cagdas D. Onal ; Daniela Rus ; Robert J. Wood Robot self-assembly by folding: A printed inchworm robot (2013) *Robotics and Automation (ICRA), IEEE International Conference*
- [11] Mirko Kovač, Jean-Christophe Zufferey, Dario Floreano Towards a Self-Deploying and Gliding Robot (2009) Chapter in *Flying Insects and Robots*, pp 271-284
- [12] N. Arora, M. U. Khan, L. Petit and C. Prelle A planar electromagnetic actuator based on two layer coil assembly for micro applications (2014) *IEEE/ASME International Conference on Advanced Intelligent Mechatronics (AIM)*
- [13] Cugat O, Delamare J, Reyne G. (2003) Magnetic micro-actuators and systems (MAGMAS). *Magnetics, IEEE Transactions on.* 39(6):3607-12.
- [14] Niarchos D. (2003) Magnetic MEMS: key issues and some applications. *Sensors and Actuators A: Physical* 109(1):166-73.
- [15] Golda, Dariusz, Design of High-Speed, Meso-Scale Nanopositioners Driven by Electromagnetic Actuators (2008), Thesis under supervision of Martin L. Culpepper
- [16] Benjamin Goldberg, Michael Karpelson, Onur Ozcan, and Robert J. Wood Planar fabrication of a mesoscale voice coil actuator (2014) *IEEE International Conference on Robotics & Automation (ICRA)*
- [17] Juan José Zárate, Giordano Tosolini, Simona Petroni, Herbert Shea Optimization of the force and power consumption of a microfabricated magnetic actuator (2015) *Sensor and Actuators A: Physical*
- [18] Pauline J Chang, Frank W Chang, Michelle C Yuen, Robert Otilar, David A Horsley Force measurements of a magnetic micro actuator proposed for a microvalve array (2014) *Journal of Micromechanics and Microengineering*, Volume 24, Number 3
- [19] T. A. T. Dang ; M. Bosch-Mauchand ; C. Prelle Modeling and simulation of a flexible path generation for an electromagnetic smart conveyance surface (2016) *International Conference on Research and Education in Mechatronics (REM)*
- [20] Muneeb Ullah Khan ; Amaury Charvet ; Jérémy Terrien ; Frédéric Lamarque ; Christine Prelle Design and thermal assessment of a micro electromagnetic actuator (2016) *International Conference on Research and Education in Mechatronics (REM)*
- [21] David B. Hiemstra, Gaurav Parmar, and Shorya Awtar Performance Tradeoffs Posed by Moving Magnet Actuators in Flexure-Based Nanopositioning (2014) *IEEE/ASME Transactions on Mechatronics*, Vol. 19, No. 1
- [22] Salerno, M., Firouzeh, A. and Paik, J. An Origami Robot-based Parallel Platform with Embedded Electro-Magnetic Actuation *ASME Journal of Mechanism and Robotics*, (submitted August 2016)
- [23] E.P.Furlani, "Permanent Magnet and Electromechanical Devices", New York: Academic.Press, 2001.
- [24] T. L. Bergman, A. S. Lavine, F. P. Incropera, D. P. Dewitt "Introduction to Heat Transfer", 7th edition, John Wiley & Sons, 2011.
- [25] Salerno, Marco, R. Rizzo, Edoardo Sinibaldi, and Arianna Mencias. "Force calculation for localized magnetic driven capsule endoscopes." In *Robotics and Automation (ICRA), 2013 IEEE International Conference on*, pp. 5354-5359. IEEE, 2013.